The Astrophysical Journal, 884:180 (14pp), 2019 October 20 https://doi.org/10.3847/1538-4357/ab3220

AGN All the Way Down? AGN-like Line Ratios Are Common in the Lowest-mass Isolated Quiescent Galaxies

Claire Mackay Dickey[1], Marla Geha[1], Andrew Wetzel[2,3,4,6], and Kareem El-Badry[5]
[1] Department of Astronomy, Yale University, New Haven, CT 06520, USA
[2] Department of Physics, University of California, Davis, CA 95616, USA
[3] TAPIR, California Institute of Technology, Pasadena, CA 91125, USA
[4] The Observatories of the Carnegie Institution for Science, 813 Santa Barbara St, Pasadena, CA 91101, USA
[5] Department of Astronomy and Theoretical Astrophysics Center, University of California Berkeley, Berkeley, CA 94720, USA
Received 2019 February 1; revised 2019 July 9; accepted 2019 July 13; published 2019 October 23

Abstract

We investigate the lowest-mass quiescent galaxies known to exist in isolated environments ($M^* = 10^{9.0-9.5}\,M_\odot$; 1.5 Mpc from a more massive galaxy). This population may represent the lowest stellar mass galaxies in which internal feedback quenches galaxy-wide star formation. We present a Keck/Echelle Spectrograph and Imager long-slit spectroscopy for 27 isolated galaxies in this regime (20 quiescent galaxies and 7 star-forming galaxies). We measure emission line strengths as a function of radius and place galaxies on the Baldwin–Phillips–Terlevich (BPT) diagram. Remarkably, 16 of 20 quiescent galaxies in our sample host central active galactic nucleus (AGN)-like line ratios. Only five of these quiescent galaxies were identified as AGN-like in the Sloan Digital Sky Survey due to a lower spatial resolution and signal-to-noise ratio. We find that many of the quiescent galaxies in our sample have spatially extended emission across the non-star-forming regions of BPT-space. While quenched galaxies in denser environments in this mass range often show no evidence for AGN activity, a significant fraction of quiescent galaxies in isolation host AGNs despite their overall passive appearances.

Key words: galaxies: active – galaxies: dwarf – galaxies: evolution

1. Introduction

Understanding the processes that regulate star formation and quench galaxies remains a major goal for studies of galaxy evolution. Since the advent of the hierarchical cold dark matter paradigm, a feedback mechanism or mechanisms have often been invoked to explain the discrepancies between the observed stellar mass function and the halo mass function (White & Rees 1978; Dekel & Silk 1986; White & Frenk 1991). Feedback mechanisms fall into two categories, processes that arise in high-density environments and those that are internal to galaxies (Peng et al. 2010). A diverse set of external phenomena (ram pressure stripping, tidal forces, major and minor mergers, etc.) are able to remove or heat gas in group and cluster environments and are particularly effective in low-mass galaxies (e.g., Pasquali et al. 2010; Smith et al. 2012). Within individual galaxies, active galactic nuclei (AGNs) appear necessary to produce the observed population of massive quenched galaxies (e.g., Croton et al. 2006; Somerville et al. 2008; Choi et al. 2015; Su et al. 2019), heating gas via high-velocity winds and radio jets. The efficiency of internal versus external quenching mechanisms is a strong function of galaxy mass; with high-mass galaxies dominated by processes internal to themselves and low-mass galaxies exclusively quenched by environmental effects (Somerville & Davé 2015).

While environmental processes can effectively quench galaxies across almost all mass regimes (the most massive galaxies being an exception; Peng et al. 2010; Wetzel et al. 2013), the efficiency of self-quenching is thought to be tightly correlated with mass. Geha et al. (2012) found that there is a stellar mass threshold below which isolated galaxies at $z < 0.055$ in the Sloan Digital Sky Survey (SDSS; Aihara et al. 2011) cannot quench themselves. They found that all of the several thousand galaxies with $M_* = 10^{7.0–9.0}\,M_\odot$ identified in SDSS as isolated (defined as 1.5 Mpc from a more massive companion), were star-forming (SF; despite the existence of quiescent galaxies in non-isolated environments in the same mass regime). Whatever process(es) act within low-mass galaxies to disrupt star formation either become inefficient or cannot occur below $M_* = 10^{9.0}\,M_\odot$. This quenching threshold is also observed to be consistent across redshift (Papovich et al. 2018). Supernovae (SNe), stellar winds, and AGN are all possible sources for driving feedback in galaxies just above this quenching threshold, but their relative impact on the evolution of low-mass galaxies remains uncertain. While it is widely agreed that AGNs are both ubiquitous and influential in massive (L^*) galaxies, a key question is whether AGNs play a role in quenching all the way down to the lowest-mass isolated quiescent galaxies.

Constraining the mechanisms responsible for quenching low-mass galaxies is challenging for a variety of reasons. The physics underlying AGN feedback remains poorly understood, such that simulations must be tuned to reproduce observed galaxy scaling relations (e.g., Bower et al. 2006; Somerville et al. 2008; Gabor et al. 2011; Genel et al. 2014; Schaye et al. 2015). Cosmological simulations are thus limited in their ability to constrain the influence of AGN, particularly in low-mass galaxies which often lie at the limits of resolution. While some zoom-in simulation studies are beginning to include isolated galaxies with $M_* = 10^7–10^9\,M_\odot$ (e.g., Graus et al. 2019), there has been minimal focus on AGN and robust observational data to test against remains sparse.

Additionally, identifying AGNs in low-mass galaxies remains difficult. Stellar or gas dynamics are the most secure method for discovering supermassive black holes (for a review see Kormendy & Kennicutt 2004), but resolution limits largely prohibit the use of this technique beyond the confines of the

[6] Caltech-Carnegie Fellow.

Local Group. In more distant systems, it is possible to identify actively accreting systems using broad Hα, which traces gas orbiting in a deep potential well (e.g., Greene & Ho 2007), and narrow emission line ratios, which can distinguish between different sources of ionizing radiation (e.g., Barth et al. 2008; Reines et al. 2013). However, broad lines alone are not a conclusive indicator of AGN activity (Baldassare et al. 2016), and narrow lines are subject to a variety of systematics and biases, discussed in more detail below.

Systematic searches rely on large spectroscopic surveys like SDSS, which are limited by the brightness of host galaxies for targeting, the strength of emission lines for identification, and contamination from the host galaxy which obscures AGN signals (e.g., Trump et al. 2015). Moreover, while Baldwin–Phillips–Terlevich (BPT) line ratios can be used to identify AGN candidates, without additional follow-up (e.g., X-ray emission, IR colors, etc.) emission cannot be conclusively identified as originating from an AGN (e.g., Yan & Blanton 2012; Belfiore et al. 2017). The BPT diagram has also been found to be less effective at identifying intermediate black holes, creating further challenges (Cann et al. 2019) for the identification of AGNs in low-mass galaxies.

Despite these challenges, the number of central black holes discovered in host galaxies with $M_* < 10^{10}\,M_\odot$ continues to grow. The discovery of individual galaxies with notably low-mass central black holes (e.g., Filippenko & Ho 2003; Barth et al. 2004; Satyapal et al. 2007; Baldassare et al. 2015, etc.) has led to more thorough searches and dedicated surveys (e.g., Greene & Ho 2007; Reines et al. 2013; Sartori et al. 2015; Baldassare et al. 2018, etc.). These studies rely on a variety of techniques, all of which suffer from observational biases (e.g., Trump et al. 2015; Agostino & Salim 2019; Cann et al. 2019). Thus, the known population of AGNs in low-mass galaxies is far from complete.

Recent studies suggest that central black holes may exert significant influence on their low-mass host galaxies. Penny et al. (2018) found a set of quiescent galaxies in group environments with both AGN-like BPT line ratios and disturbed gas kinematics, suggesting AGN-driven outflows. Bradford et al. (2018) studied the H I gas masses of isolated low-mass galaxies with BPT-identified AGNs and found two populations; composite galaxies with gas content in line with non-AGN galaxies, and gas-depleted galaxies with stronger AGN signatures. They suggest that AGNs may be able to affect the cold gas content of some galaxies with low stellar masses.

These studies exist in some tension with other work which suggests that stellar and SNe feedback, rather than black hole accretion, are the dominant forces which moderate star formation in low-mass galaxies (e.g., Bower et al. 2017; Martín-Navarro & Mezcua 2018).

In this work, we investigate the processes required to quench isolated galaxies, focusing on the lowest-mass galaxies that are isolated and lack recent star formation. We define galaxies as SF or quiescent based on observational properties as measured by the SDSS fiber spectroscopy. We consider galaxies to be quiescent if they have both old stellar populations and sufficiently low levels of star formation. We intentionally differentiate between quenched galaxies in which star formation has been fully and permanently disrupted and quiescent galaxies which are not currently forming stars but are not necessarily "dead."

We discuss the observational proxies and exact definitions used in Section 2 and build a catalog of isolated low-mass galaxies. We present new Keck/Echelle Spectrograph and Imager (ESI) long-slit spectroscopy for a subset of these galaxies. In Section 3 we measure emission line fluxes for galaxies as a function of radius and place them on the BPT diagram, categorizing individual galaxy spaxels as quiescent, SF, AGN-like, or composite. We identify central AGN candidates and classify the radial trends of galaxies on the BPT diagram. In Section 4, we measure the perpendicular distance from the SF region in [O III]/Hβ versus [N II]/Hα space, and connect this indicator of the relative strength of non-SF ionizing radiation to host galaxy properties. We summarize our work and its implications in Section 7. We assume $H_0 = 70\,\mathrm{km\,s^{-1}\,Mpc^{-1}}$ throughout this work.

2. Data

2.1. Galaxy Catalog and Isolation Criterion

The parent sample for this work is the NASA/Sloan Atlas[7] (NSA; Blanton et al. 2011), a reanalysis of SDSS DR8, optimized for nearby low-luminosity objects. The NSA galaxy catalog includes fluxes, optical line strengths and equivalent widths (EWs), and associated errors for all objects derived using the methods of Yan & Blanton (2012) and the SDSS spectrophotometric recalibration of Yan (2011). The catalog also includes stellar masses, estimated with the `kcorrect` software (Blanton & Roweis 2007), based on SDSS optical fluxes as well as *Galaxy Evolution Explorer* fluxes where available, and assuming a Chabrier (2003) initial mass function (IMF).

Following Geha et al. (2012), we define galaxies as isolated based on the quantity $D_{\rm host}$, the projected distance to the nearest "luminous" neighbor, where luminous is defined to be $M_{K_s} < -23$ (corresponding to $M_* = 2.5 \times 10^{10}\,M_\odot$). Luminous galaxies are considered to be potential host galaxies if they are within $1000\,\mathrm{km\,s^{-1}}$ in redshift and within a projected comoving distance of 7 Mpc. $D_{\rm host}$ is given as the shortest distance to a luminous neighbor within the search parameters. For the small number of galaxies where no luminous neighbor was identified, $D_{\rm host}$ was set to 7 Mpc. We consider a galaxy to be isolated if $D_{\rm host} > 1.5$ Mpc.

We focus on galaxies ± 0.5 dex around the isolated quenching threshold for a mass range of $M_* = 10^{8.5}$–$10^{9.5}\,M_\odot$ (Geha et al. 2012). The NSA catalog contains $N = 6850$ isolated galaxies within this mass range.

Our definition of isolated selects for galaxies that are centrals rather than satellites, but does not discriminate based on large scale environment, unlike other measures (e.g., 3rd or 7th nearest neighbor, aperture counts, etc.). Our galaxies all live well beyond the virial radius of their nearest neighbor, but are not necessarily living in true cosmic voids (van de Weygaert & Platen 2011).

Within this sample, we further define galaxies as quiescent, quasi-quiescent, or SF. We consider a galaxy to be quiescent based on two criteria measured from the SDSS fiber spectra: the Hα EW, which traces the specific star formation rate over the last $\sim$10–20 Myr, and the D_n4000 index, which is a measure of the light-weighted age of the stellar population and is based on the strength of the 4000 Å break (Balogh et al. 1999). Quiescent galaxies are those with Hα EW < 2 Å and $D_n4000 > 0.6 + 0.1 \cdot \log_{10}(M_*)$. We base these definitions on the empirical delineations between SF and quiescent populations in Geha et al. (2012). We remove 192 galaxies from the sample with

[7] http://www.nsatlas.org

poorly measured D_n4000 ($D_n4000_{err} > 0.1$). In the mass range $M_* = 10^{8.5}$–$10^{9.5}\,M_\odot$, the majority of galaxies (6470/6658) are defined as SF and just 11 are quiescent, consistent with Geha et al. (2012). There are an additional 177 galaxies which we define as "quasi-quiescent" because they fulfill only one of our criteria for quiescence (large D_n4000 and intermediate Hα EW, or low D_n4000 and low Hα EW) based on their SDSS fiber-based spectroscopy. These galaxies are potential analogs to the Green Valley observed at higher stellar masses.

2.2. Keck/ESI Observations

From the above sample, 27 isolated galaxies were observed over four nights (2014 March 6,7, 2015 January 19, and 2016 February 14) with the ESI (Sheinis et al. 2002) on the Keck II 10 m telescope.

In building our sample, we focused primarily on maximizing the number of quiescent galaxies observed, acquiring ESI observations for 10 of 11 quiescent galaxies, and an additional 10 of 177 quasi-quiescent galaxies which may be in the process of transitioning from star formation to quiescence. Finally, we also observed 7 galaxies that span the full range of D_n4000 and Hα EWs observed in SF, low-mass galaxies in SDSS (Figure 1, blue stars). Stellar masses, redshifts, D_n4000 and Hα EW for each observed galaxy are given in Table 1. The observed galaxies in each subsample all have similar redshift distributions to the parent sample.

The observations were taken in echellette mode, which provides wavelength coverage over the range 3900–11000 Å, across 10 echelle orders. The observations were made using the $1\farcs0 \times 20''$ slit, which gives an instrumental resolution of 32 km s^{-1} (Gaussian σ) over the full spectrum or $R \approx 10{,}000$. For each galaxy, the slit was aligned along the major-axis and a minimum of three consecutive 5 minute exposures were obtained. We achieve $\langle S/N \rangle \sim$ 10–25 pix^{-1} in the continuum across the Ca III region.

The ESI data were processed using the `XIDL` package[8] (Prochaska et al. 2003), following the ESIRedux cookbook to process the darks, flats, and arc images. The flat field images were used to trace the edges of the slit across each curved order and to correct gain mismatch across the amplifiers. From the individual arc images taken on each night, a master CuAr +HgNe+Xe arc image was created. From this master arc image the wavelength solution was derived for each night of observations.

Once the individual science frames were dark-subtracted and flat-fielded, cosmic-rays were identified and removed with the routine `LACosmic` (van Dokkum 2001). The individual science frames were median-combined and then the initially curved individual orders rectified.

To model the contribution from sky lines and continuum, we performed a B-spline fit to a 2″-wide region on the outer edges of the two-dimensional (2D) spectrum. In some cases, emission lines from the galaxy extend across the full slit (e.g., NSA 112551 in Figure 2). For these galaxies, we use the internal rotation of the galaxy to select uncontaminated regions of sky on the opposite side of the slit. For the few galaxies with negligible rotation, we assume a flat sky continuum and fit to the regions directly surrounding the emission lines in wavelength space.

[8] https://www2.keck.hawaii.edu/inst/esi/ESIRedux/index.html

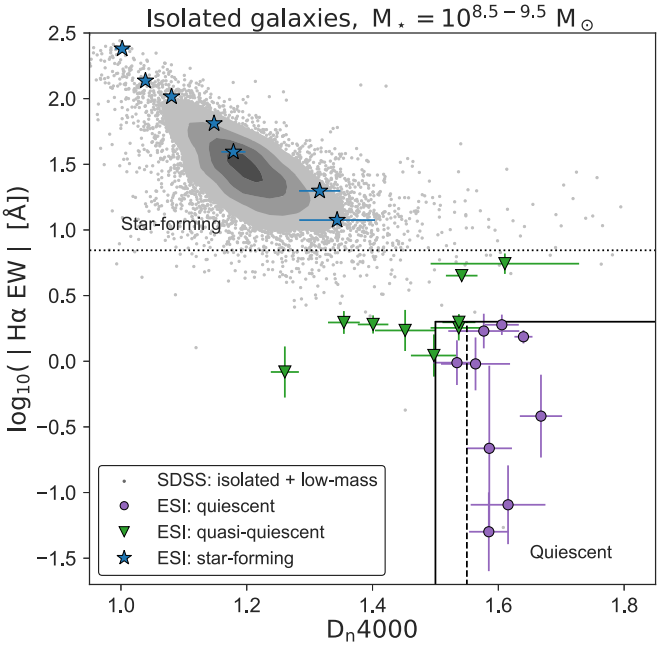

Figure 1. D_n4000 vs. Hα equivalent width for isolated ($D_{host} > 1.5$ Mpc), low-mass ($M_* = 10^{8.5}$–$10^{9.5}\,M_\odot$) galaxy sample (gray points, contours), measured with SDSS. Galaxies for which we have obtained Keck/ESI spectroscopy are shown as colored points and divided into three types based on the strength of their 4000 Å breaks and Hα EWs: SF (blue stars), quasi-quiescent (green triangles), and quiescent (purple circles). Solid lines indicate the criteria for quiescence (D_n4000 has a mass dependence, and we show the highest-mass limit with a dashed line). Galaxies are considered to be quasi-quiescent if they lie below the dotted line.

2.3. Emission Line Measurements

We are interested in measuring the strength of emission lines in low-mass isolated galaxies such that we can isolate AGN-like line ratios. However, the majority of galaxies in our sample are dominated by the stellar absorption continuum. For accurate measurements of Hα and Hβ emission, it is necessary to model and remove the effects of stellar absorption.

For each galaxy in the sample, we fit the stellar continuum from the spectrum extracted within the central 1″ (as determined from the median stellar continuum profile at $\lambda = 8400$–8800 Å). After masking the strong optical emission lines, we convolve a set of empirical stellar templates with a velocity profile using Penalized Pixel-Fitting (pPXF; Cappellari 2017) and fit to the central galaxy spectrum.

We have tested pPXF's ability to accurately recover the shape of the Balmer absorption lines by modeling a set of quiescent galaxies with and without emission line region masking. In all cases, the model produced by fitting to the line-masked spectrum is in good agreement with the model fit to the unmasked spectrum.

We assume that the relative line strength of the absorption features do not vary significantly as a function of radius. Given the stellar continuum derived from the continuum normalized central 1″, we use the median galaxy light profile to produce a 2D map of the galaxy continuum.

We subtract the galaxy continuum model from the 2D sky-subtracted spectra to correct for stellar absorption. This produces a 2D emission-line-only spectrum, from which we can extract spatially resolved 1D spectra for each galaxy. The central spectrum is centered on the peak of the galaxy

Table 1
Isolated Low-mass Galaxies Observed with ESI

ID	α J2000.0	δ J2000.0	cz (km s^{-1})	Galaxy Type	Mass ($M_\odot$)	Hα EW (Å)	D_n4000	BPT Type	d_{BPT} (dex)
NSA 81964	15:37:39.6	26:15:07.9	6654	SF	9.10	64.7	1.14	AGN	0.34 ± 0.02
NSA 71202	14:23:29.4	11:02:40.8	10414	SF	9.14	11.89	1.34	AGN	0.30 ± 0.06
NSA 76069	13:38:42.5	14:34:43.3	12747	SF	9.20	240.0	1.00	SF	0.08 ± 0.01
NSA 84573	08:59:35.0	26:48:14.3	1373	SF	9.20	39.3	1.17	SF	0.16 ± 0.02
NSA 112551	11:29:27.5	24:09:55.1	9789	SF	9.25	19.8	1.31	SF	0.08 ± 0.02
NSA 77944	13:28:04.8	06:15:57.7	9710	SF	9.30	136.8	1.03	SF	0.21 ± 0.02
NSA 66890	11:16:09.7	06:02:47.0	11792	SF	9.44	103.6	1.08	SF	0.14 ± 0.01
NSA 55500	11:06:38.2	43:23:44.5	6199	qQ	8.69	1.97	1.35	AGN	0.55 ± 0.07
NSA 89958	12:48:19.0	35:12:40.3	6836	qQ	8.99	5.53	1.61	SF	0.13 ± 0.11
NSA 67565	14:02:21.2	36:36:06.5	6995	qQ	9.12	1.10	1.49	AGN	0.57 ± 0.08
NSA 106991	10:04:23.3	23:13:23.3	7971	qQ	9.18	4.48	1.54	AGN	0.52 ± 0.04
NSA 91686	11:04:39.8	36:39:22.6	6325	qQ	9.25	0.82	1.26	AGN	0.89 ± 0.33
NSA 15814	08:13:54.0	42:45:19.4	9306	qQ	9.38	6.25	1.99	AGN	0.19 ± 0.06
NSA 61814	13:42:38.6	46:31:40.3	9205	qQ	9.39	1.71	1.45	SF	0.27 ± 0.24
NSA 78759	14:12:43.7	08:22:16.0	8567	qQ	9.44	1.91	1.40	AGN	0.53 ± 0.13
NSA 35979	08:20:13.9	30:25:03.0	5885	qQ	9.46	1.98	1.53	AGN	0.59 ± 0.04
NSA 26085	07:37:29.2	30:16:04.2	1048	qQ	9.47	1.79	1.53	AGN	0.52 ± 0.05
NSA 122277	15:08:10.8	16:05:26.7	7327	Q	9.01	0.97	1.53	AGN	0.45 ± 0.10
NSA 120659	14:31:55.1	15:02:26.7	8291	Q	9.29	0.38	1.66	AGN	1.07 ± 0.33
NSA 3478	12:27:34.7	−01:46:45.7	7391	Q	9.31	0.21	1.58	Q	⋯
NSA 51306	14:07:27.8	46:57:03.3	7851	Q	9.32	−0.05	1.58	AGN	1.07 ± 0.27
NSA 6831	01:38:42.8	00:20:53.0	5084	Q	9.33	1.89	1.60	AGN	0.77 ± 0.04
NSA 26385	08:21:23.6	41:42:26.9	7375	Q	9.37	0.98	2.01	AGN	1.21 ± 0.24
NSA 8762	01:31:28.7	13:37:52.5	9043	Q	9.41	0.95	1.56	AGN	0.57 ± 0.10
NSA 20626	16:23:35.0	45:44:43.4	1844	Q	9.41	1.53	1.63	AGN	1.19 ± 0.15
NSA 119887	12:30:31.3	25:18:34.2	6680	Q	9.43	1.69	1.57	AGN	0.77 ± 0.24
NSA 18953	15:45:16.9	02:22:54.2	1173	Q	9.46	−0.08	1.61	Q	⋯

Note. Galaxy type, mass, Hα EW, and D_n4000 are all derived from the SDSS fiber, while BPT type and d_{BPT} are measured from the central 1″ of the ESI spectra.

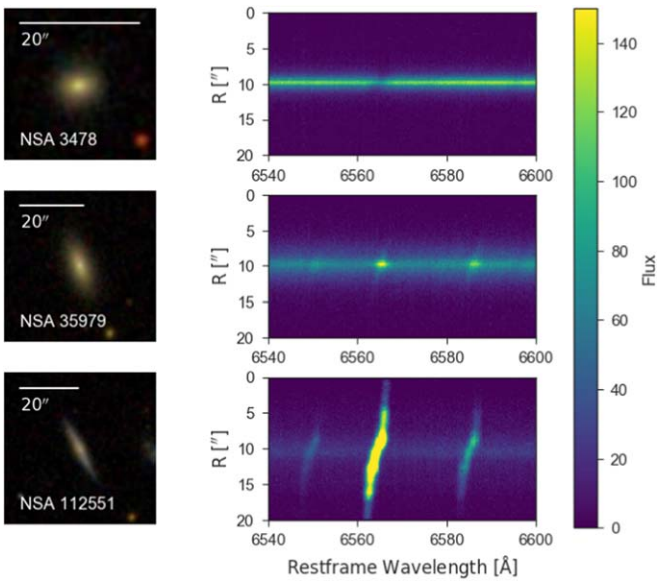

Figure 2. SDSS *gri* images for three galaxies in our sample (left), and corresponding sky-subtracted 2D Keck/ESI spectra for each galaxy, centered on the Hα + [N II] region (right). Galaxies in our sample show a variety of emission line profile behaviors, with some dominated by stellar absorption (top), some showing only centrally concentrated emission (middle), and some with emission line extending across the full slit (bottom). All galaxies shown here have similar stellar masses ($M_* \sim 10^{9.2-9.4}\,M_\odot$).

brightness profile and extracted from a 1″-wide region (corresponding to the average seeing across our nights). Successive spectra are extracted at increasing radii with a width of 1″.

Given a set of spectra for each galaxy, we follow Reines et al. (2013) and model the emission lines of interest as Gaussians. We initially fit the Hα + [N II] region, keeping the relative separations fixed at their laboratory wavelengths and the flux ratio of [N II] λ6583 to [N II] λ6548 at the intrinsic ratio of 2.96. We then measure the [S II] $\lambda\lambda$6718,6732 doublet, Hβ, and the [O III] $\lambda\lambda$4959,5007 doublet, while fixing the model to Hα + [N II] linewidth and velocity.

We also test for the presence of a broad Hα component by refitting the Hα + [N II] region, allowing for an additional broad Gaussian in the Hα line with an FWHM of at least 500 km s^{-1}. We consider the fit to be improved if the χ^2 decreases by 25%, but do not find any evidence of broad Hα for any galaxies within our sample.

3. Placing Galaxies on the BPT Diagram

The BPT diagram (Baldwin et al. 1981) is a powerful diagnostic for differentiating between the sources of ionizing radiation in a galaxy spectrum (Veilleux & Osterbrock 1987; Kewley et al. 2001, 2006; Kauffmann et al. 2003a). While there are many variations on the original optical line ratio diagram

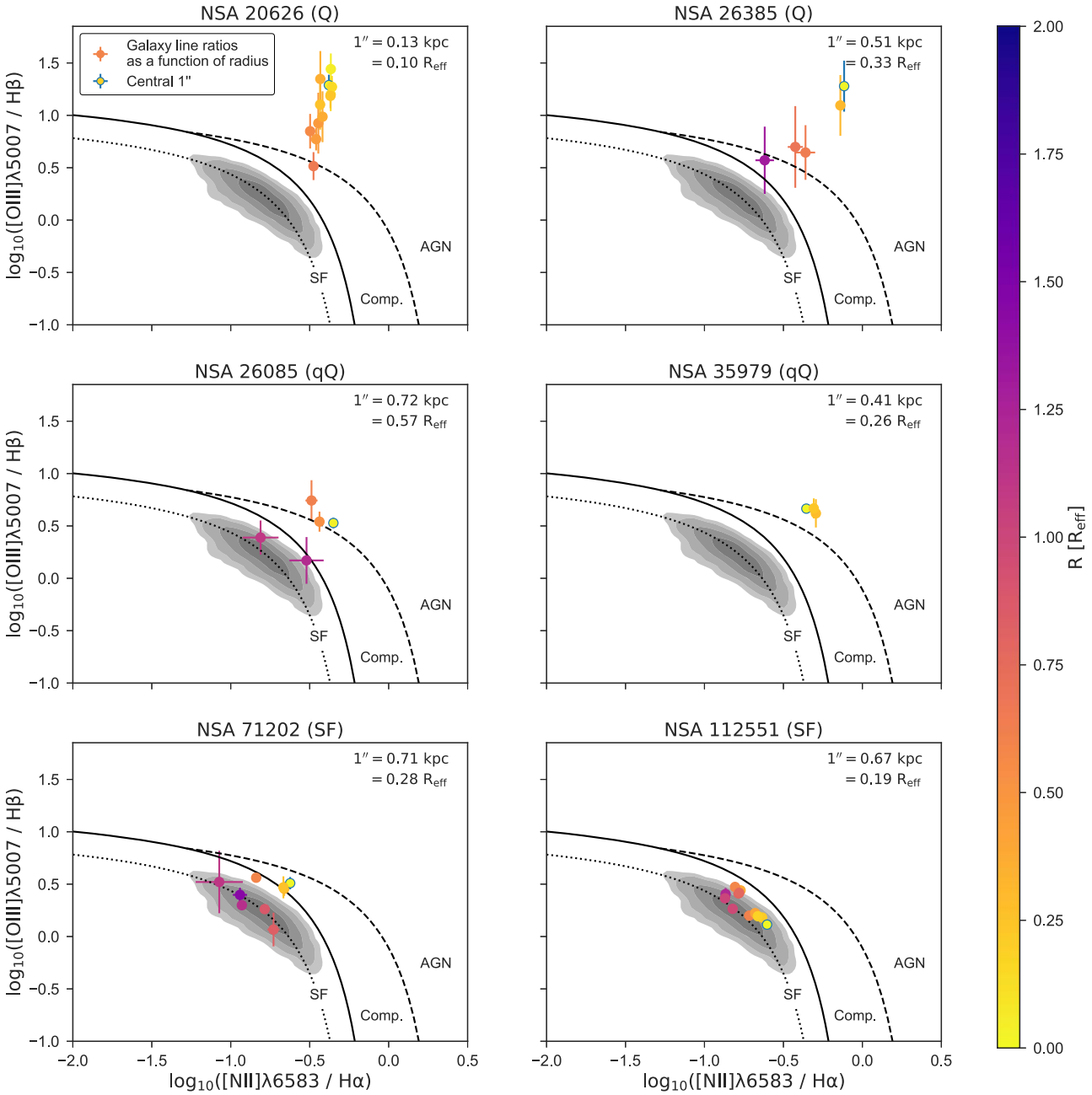

Figure 3. A selection of BPT diagrams for six galaxies in our sample which highlight the observed spatial patterns within each galaxy subtype. Each panel shows the locus of low-mass isolated galaxies with well-measured BPT emission lines (Hα and Hβ S/N $>$ 3) from the NASA/Sloan Atlas (NSA; gray contours) as well as the demarcation lines between sources of ionizing radiation as given in Kewley et al. (2013), where the dotted line traces the median H II abundance sequence, the solid line is the empirical delineation between star formation and AGN (Kauffmann et al. 2003a), and the dashed line is the maximum-starburst line (Kewley et al. 2001). We show BPT measurements derived from the ESI spectra as circles, color-coded by distance from the galaxy center. Points are outlined in blue when they lie within the central arcsec of the galaxy. Galaxies fall into three broad categories: dominated by star formation (bottom row), central AGN with extended SF (top right, middle right), and pure AGN (top left). 16/20 galaxies defined as quiescent based on their D_n4000 and Hα EWs show signatures of AGN, along with two of seven SF galaxies.

and many classification schemes therein, we focus on the "traditional" BPT, which uses the ratios [N II]/Hα versus [O III]/Hβ.

In this space, SF galaxies which are dominated by emission from H II regions create the sequence marked by a dotted line in each panel of Figure 3 (the SF sequence; Kewley et al. 2013). Lower metallicities produce higher [O III]/Hβ ratios and lower [N II]/Hα ratios (Groves et al. 2006; Kewley et al. 2006; Cann et al. 2019).

We follow the commonly used classification scheme for distinguishing between sources of ionizing radiation (star formation versus AGN, shocks, or post-asymptotic giant branch (pAGB) stars; e.g., Kewley et al. 2006, 2013; Reines et al. 2013; Baldassare et al. 2018). The dashed line in Figure 3 from Kewley et al. (2001) represents the division between a theoretical maximum-starburst model versus emission that requires a harder ionizing spectrum (e.g., AGN activity). The Kauffmann et al. (2003a) division (solid line in Figure 3) is an

empirical separation between the SF sequence and the AGN plume, which extends to larger [N II]/Hα and [O III]/Hβ ratios. Galaxies below the Kauffmann et al. (2003a) demarcation are considered to be purely SF, while galaxies above the Kewley et al. (2001) are traditionally considered to be Seyfert AGN and low-ionization nuclear emission regions (LINERs). Galaxies lying between these two regions are considered to be composites, whose spectra suggest a mix of ionization from star formation and harder radiation.

The BPT diagram is primarily used for identifying AGN activity in galaxies, as the harder ionizing radiation from an actively accreting supermassive black hole produces line ratios distinct from those found in a SF galaxies. However, there are several other astrophysical process that can produce line ratios similar to those from AGN. In general, BPT line ratios alone are insufficient to rule out other ionization mechanisms, like SNe shocks or heating from pAGB stars (Yan & Blanton 2012; Yan 2018).

3.1. Comparison with SDSS

We first compare the SDSS 3″-fiber flux ratios to those measured from our ESI spectra. We only evaluate the SDSS BPT diagram for a galaxy where the flux measurements have sufficient signal-to-noise ratio (S/N) in the four key lines (Hα, Hβ, [O III], and [N II] S/N > 3). Of the 27 galaxies in our sample, only 12 have reliably measured BPT flux ratios in SDSS.

For each of the 12 galaxies, we extract a 3″ diameter spectrum from across the ESI slit, centered on the peak of the stellar continuum. The ESI extraction is matched to SDSS in diameter but not area (due to the mismatch of fiber versus long slit). Still, for all 12 galaxies, we confirm the SDSS BPT classifications within $R = 3''$ centered on the peak of the stellar continuum in our ESI data, although we show in Section 3.2 that this varies with smaller apertures.

3.2. Spatially Resolved BPT Diagrams

The Keck/ESI spectrograph provides up to 20″ of spatial information on each galaxy in our sample, with ∼1″ resolution. In Figure 3, we present spatially resolved BPT diagrams for a subset of galaxies in our sample (BPT diagrams for the full sample are included in the Appendix).

The galaxies in our sample were originally classified as SF (7/27), quiescent (10/27), or quasi-quiescent (10/27) based on the SDSS fiber measurements of their stellar populations (Hα EW and D_n4000, as shown in Figure 1).

In the seven galaxies defined as SF, the emission lines extend across the full 20″ slit (e.g., NSA 112551, bottom row in Figure 2). All seven galaxies are classified as BPT-SF (emission originating from H II regions) from the 3″ spectra, but two of seven galaxies have composite line ratios within the central 1″, suggesting contribution to the emission from a non-SF-driven source of hard ionizing radiation. For the remaining five galaxies, the line ratios at all radii are consistent with ionizing radiation originating exclusively from star formation .

Though all seven SF galaxies are broadly classified as BPT-SF at (almost) all radii, the distribution of the emission line ratios within BPT-SF space as a function of radius varies from galaxy to galaxy. For three of the seven galaxies the line ratios at all radii are loosely clustered, with no clear radial trends.

In contrast, three galaxies show large radial variations in [N II]/Hα (e.g., NSA 112551 in Figure 3). In two cases, the [N II]/Hα ratio is greater at the center of the galaxy and decreases at larger radii, while the third galaxy (NSA 84573, see Figure 9) has [N II]/Hα ratios that increase with radius, while still remaining within the SF region. For all three galaxies, [O III]/Hβ is approximately constant as a function of radius. The galaxies not included in Figure 3 are shown in the Appendix.

Before examining the radial trends for quiescent and quasi-quiescent galaxies, we model the effects of key stellar population parameters on BPT-position, to better disentangle the behavior of underlying galaxy properties from any possible AGN contributions. The quiescent and quasi-quiescent galaxies will be discussed below in Section 3.3.

3.3. Modeling BPT-behavior with Simple Stellar Populations

To better understand how galaxies move through BPT-space, we investigate the effects of varying the stellar age, metallicity, and contribution from AGN to the emission line spectra for a set of simple stellar populations. We use `FSPS` (Conroy et al. 2009; Conroy & Gunn 2010) to generate spectra for simple stellar populations, varying both stellar age and metallicity (solid lines in Figure 4, upper panel). We assume a Kroupa (2001) IMF and set the gas-phase metallicity to match the stellar, with a fixed gas ionization parameter of $\log(U) = -2.0$. Nebular emission lines are generated for a given SSP as described in Byler et al. (2017).

Actively SF galaxies (those with the youngest stellar ages, white-faced circles in Figure 4) lie along the median H II abundance sequence. Increasing metallicity moves the spectrum to larger [N II]/Hα at nearly constant [O III]/Hβ.

The distribution of our simple stellar populations through BPT-space suggest that metallicity gradients as a function of radius can explain the horizontal sequences observed in some of the SF galaxies. Some cosmological zoom-in simulations predict that potential fluctuations from stellar feedback in low-mass galaxies can drive negative metallicity gradients ($\Delta \log Z/Z_{M_\odot} \sim -0.25$, El-Badry et al. 2016), which are echoed by MaNGA observations that have found flat to slightly negative metallicity gradients in low-mass galaxies (Belfiore et al. 2017).

We also model the AGN narrow line spectrum as a set of Gaussian emission lines. Metallicity, gas density, and ionization parameter can all influence the narrow line region (NLR) and the resulting BPT diagram position. We select our underlying AGN line ratios such that the "AGN" lies in the Seyfert region of the BPT diagram, while the Hα and Hβ ¯uxes are scaled to 10%–100% of the SF fluxes. The location of an AGN on the BPT diagram also depends on the black hole mass and Eddington ratio, which can lead to AGNs lying in the SF region of BPT-space in some extreme cases (Cann et al. 2019). Given our observations of Seyfert-like line ratios in many of our galaxies, we use Seyfert-like ratios in our model.

Increasing the flux contribution from the AGN relative to the star formation produces the curved diagonal tracks shown in Figure 4 (lower panel, dashed and dotted–dashed lines). The curvature of these tracks varies with both the metallicity and time elapsed since star formation, as well as the fundamental line ratios of the AGN. We show how the emission line ratios evolve with increasing AGN fraction for a Seyfert AGN (Figure 4, bottom panel). While this is a toy model, it suggests

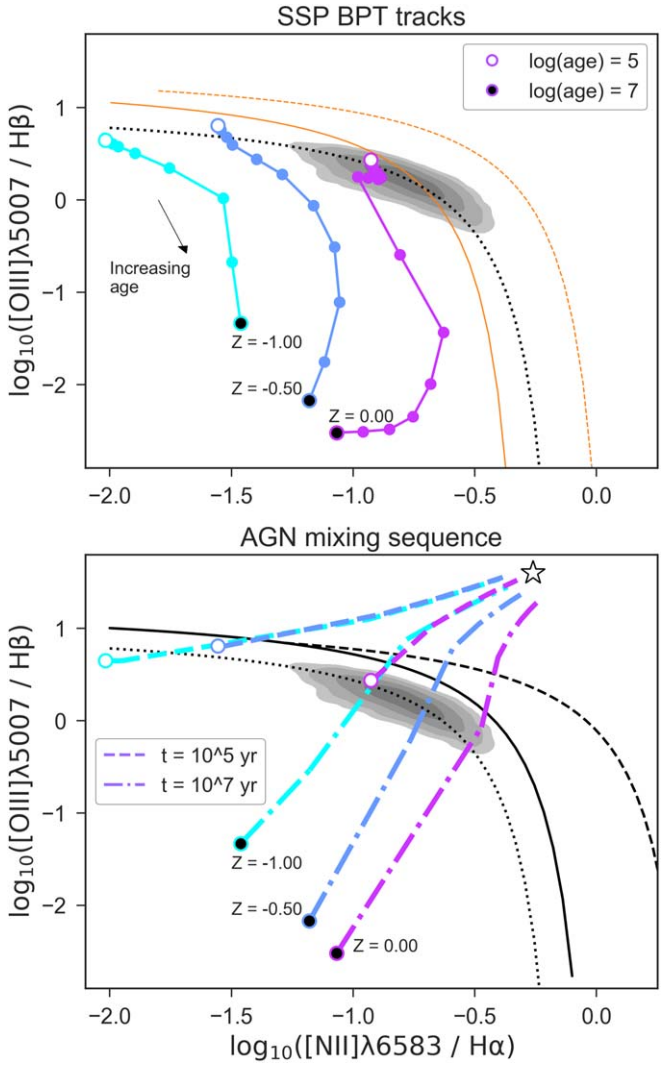

Figure 4. Upper panel: the evolution of simple stellar populations in BPT-space as a function of stellar age (solid lines) and metallicity (blue-purple). Increasing metallicity moves galaxies to larger [N II]/Hα, while older stellar populations have lower [O III]/Hβ. The orange lines show the effect of increasing the ionization parameter (solid) and electron density (dashed) on the SF locus (adapted from Kewley et al. 2013.) Lower panel: the effect of adding Seyfert AGN-like emission to a simple stellar population. Dot–dashed lines show the effect of increasing AGN contribution at fixed age and metallicity for the underlying stellar population. The AGN fraction increases from 0% to 90% toward the upper right. The white star marks our fiducial AGN ratios.

that variation in the contribution from an AGN produces diagonal sequences which are distinct from the horizontal sequences driven by metallicity gradients.

In the upper panel of Figure 4 we also show the effect of increasing the ionization parameter (solid orange line) or the electron density (dashed orange line) on the SF abundance sequence (dotted black line), adapted from Figure 2 of Kewley et al. (2013). Increasing the electron density can move SF galaxies into the composite region, while a larger ionization parameter can variously decrease [N II]/Hα or increase [O III]/Hβ depending on location along the SF sequence.

Of the 10 quasi-quiescent galaxies (green triangles, Figure 1), six have evidence for some ongoing star formation within the slit. However, only one of these six galaxies is purely SF in BPT-space; the five other galaxies show evidence of emission originating from a non-SF source within $\sim$0.5 $R_{\rm eff}$ (e.g., NSA 26085, center-left in Figure 3). In all four of the remaining quasi-quiescent galaxies, we only observe emission that is consistent with a non-SF source of ionizing radiation (e.g., NSA 35979, center-right in Figure 3).

Finally, our sample includes 10 quiescent galaxies (purple circles in Figure 1). Of those 10, we find two galaxies (NSA 3478 and 18953) to be fully quiescent systems, with no detected emission at any radii. Of the eight remaining galaxies for which we can measure the BPT line ratios, only one galaxy (NSA 119887) shows emission consistent with star formation. Visual inspection of the galaxy in SDSS *gri* shows a possible off-center H II region. Given the small spatial extent and weakness of the Hα flux from the SF region relative to central non-SF source, we still consider this galaxy to be predominantly quiescent.

The seven other quiescent galaxies exclusively inhabit the composite and AGN-like regions of the BPT diagram, with no evidence of purely SF line ratios at any radii.

In 12 of 15 quiescent and quasi-quiescent galaxies with non-SF line ratios, the AGN-like emission extends beyond the central 1″. In most cases, AGN-like or composite line ratios are observed out to $R \sim 0.5\,R_{\rm eff}$.

Of the galaxies that appear to host non-SF-like ionizing radiation, 8/18 show strong variation in their line ratios as a function of radius. In each of these cases, the galaxy moves diagonally through BPT-space, with both [N II]/Hα and [O III]/Hβ increasing toward the galaxy center (e.g., NSA 26385, top right in Figure 3).

In the case of NSA 20626 (top left, Figure 3), the emission line ratios create a nearly vertical sequence in BPT-space. Increasing the AGN contribution to the spectrum always changes both the [O III]/Hβ and [N II]/Hα, suggesting that the near-vertical sequence observed in NSA 20626 cannot be explained exclusively by variation in the ratio of star formation to AGN present in the galaxy. We note that NSA 20626 is an extreme case, being more nearby ($z = 0.006$) and larger in size ($R_{\rm eff} = 9\farcs71$) than other galaxies in the sample, allowing us to probe a much smaller region of the galaxy center at improved resolution. However, the remaining quiescent galaxies in our sample all lie within the same redshift range as the SF galaxies, confirming that the observed differences between the populations are not an effect of resolution.

To summarize, we have examined the radial behavior of galaxies on the BPT diagram and found that the majority of quiescent and quasi-quiescent galaxies have extended AGN-like line ratios which form characteristic diagonal tracks across BPT-space, which are distinct from the metallicity gradients observed in SF galaxies.

3.4. The Central 1″

Our investigation of the spatially resolved BPT diagram for low-mass galaxies shows that the excitation contribution from non-SF sources can vary significantly as a function of radius, but always peaks within the central arcsecond of each galaxy. A possible explanation for this behavior is that we are observing the increasing influence of AGN activity within each galaxy's NLR.

To better quantify the influence of the harder ionizing radiation present within our sample of galaxies, we focus on only the central 1″ of each galaxy, where emission from an AGN, if present, should dominate. Based on the BPT

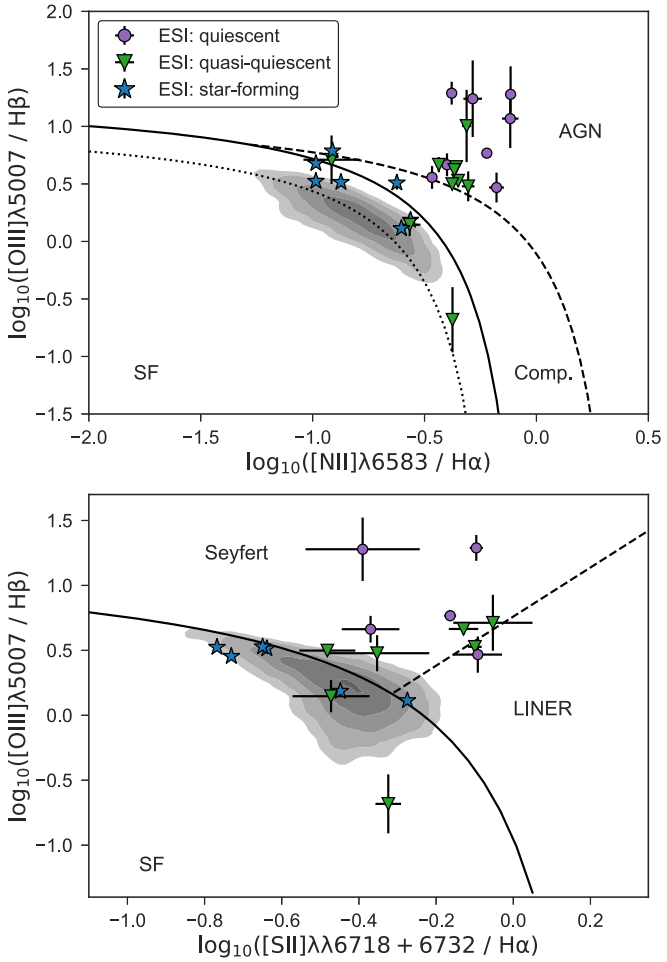

Figure 5. Upper panel: the [N II]-BPT diagram for all galaxies in the sample, measured within the central 1″ of the Keck/ESI spectra. Galaxies classified as SF from their stellar populations in SDSS (blue stars) lie in the SF or composite regions of the BPT diagram. Quiescent and quasi-quiescent galaxies (circles and triangles) lie primarily in the AGN region of the diagram. Lower panel: the [S II]-BPT diagram for a subset of galaxies within the sample, once again measured within the central 1″ of the Keck/ESI spectra. The [S II]-BPT diagram can be used to distinguish between Seyfert AGN and low-ionization nuclear emission regions (LINERs), which may have more ambiguous origins.

classifications of Kewley et al. (2006), we classify the central 1″ as quiescent, AGN-like, or SF (Table 1, BPT type). The BPT diagram traditionally distinguishes between the "AGN" and "composite" regions, where composite refers to a mix of star formation and AGN-driven ionization, but this is a empirical divide, calibrated to high-mass galaxies.

BPT line ratios are not an unbiased tracer of AGN activity, as the presence of even small amounts of star formation can "dilute" AGN-like line ratios (Trump et al. 2015). Recent work suggests that the underlying ionizing spectrum for of intermediate mass black holes may never produce line ratios in the composite or AGN regions (Cann et al. 2019). We note that the SF galaxy sample extends to lower stellar masses than the quiescent one, potentially heightening this effect. Therefore, we cannot rule out the presence of hidden AGN in the SF galaxies.

Figure 5 shows the position of each galaxy's central 1″ on the [N II] and [S II] BPT diagrams (upper and lower panels, respectively). SF galaxies lie near the H II sequence (dotted line, upper panel). The small number of SF galaxies with AGN-like line ratios all lie very close to or within the composite region, suggesting low-metallicity gas (Groves et al. 2006), a significant contribution from star formation in the central 1″, or both.

In SDSS, galaxies not classified as SF are primarily found in the composite region, where we expect to see galaxies with a mix of star formation and AGN emission. Within the ESI central 1″, almost none of the quiescent and quasi-quiescent galaxies lie in this composite region, suggesting that either there is no underlying star formation at the smallest radii or that we are probing the region where the harder ionizing radiation is strong enough to dominate over any residual star formation.

Additionally, we find that the majority of our AGN-like galaxies lie in the Seyfert region of the [N II] BPT diagram, making it less likely that the emission in these galaxies originates from pAGB stars, which are predominately LINER-like. Placement on the [O I] BPT diagram could further distinguish between shocks and AGN, but we are unable to recover [O III]-6300λ in our spectra.

The majority of the quiescent and quasi-quiescent galaxies in our sample lacked sufficient S/N for placement on the BPT diagram with SDSS. In 13 of the 15 galaxies that did not have SDSS BPT measurements, the increased spectral and spatial resolution of the Keck/ESI spectra reveals the presence of faint central emission consistent with AGN-like line ratios.

Of the 20 galaxies defined as quiescent or quasi-quiescent based on their stellar populations, we find that 16 show evidence of potentially hosting an actively accreting central black hole.

4. BPT Distance and Quiescence

Thus far, we have examined how our galaxies would be defined within the traditional BPT diagram. However, this classification scheme has been calibrated for galaxies more massive than our sample. Low-mass galaxies have weaker AGN emission relative to their high-mass counterparts, and their metal-poor nature can significantly influence their position on the BPT diagram, as metallicity is a significant driver of BPT-position for both star formation and AGN-dominated spectra, as we have shown in Section 3.3. Due to these complicating factors, we find it useful to parameterize each galaxy's relative position on the BPT diagram. We use $d_{\rm BPT}$, the perpendicular distance from the Kewley et al. (2013) SF sequence (Figure 5, dotted line) as measured for the central 1″ ESI spectrum of each galaxy.

We compare $d_{\rm BPT}$ to D_n4000, which measures the strength of the 4000 Å break and serves as a good proxy for the age of stellar populations. We use stellar age as traced by D_n4000 rather than any proxy for star formation , as we cannot decouple Hα emission originating from H II regions versus that from other sources. Our ESI spectra lack the required sensitivity in the bluest orders to measure D_n4000, so we rely on the values derived from the 3″ SDSS fiber. Simulations predict moderate age gradients in low-mass galaxies ($\Delta t \sim 1$ Gyr within 1 kpc; El-Badry et al. 2016). For quiescent galaxies, where we expect older overall ages, D_n4000 does not vary significantly on Gyr timescales and should have similar values when measured within 1 versus 3″.

In Figure 6 we find a correlation between $d_{\rm BPT}$ and D_n4000, with the oldest galaxies most removed from the BPT SF sequence. AGNs found in SF galaxies are found significantly

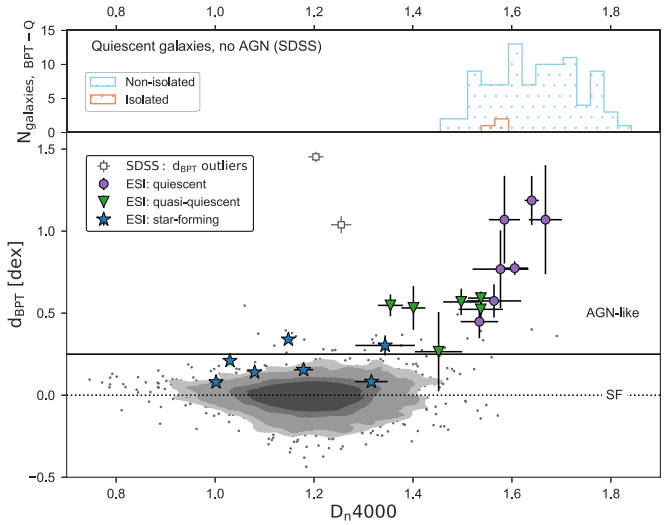

Figure 6. Lower panel: $d_{\rm BPT}$ as a function of D_n4000 for isolated, low-mass galaxies in SDSS (gray) and galaxies observed with ESI (colors). The D_n4000 index measures the strength of the Balmer break and is a good proxy for stellar age, with large values of D_n4000 indicating an evolved stellar population. Large BPT distances indicate stronger ionizing radiation signatures, while $d_{\rm BPT} = 0$ indicates a galaxy is on the median SF sequence. We find that the BPT-position of the central 1″ in a galaxy is tightly correlated with the age of the galaxy. White squares mark two outliers from SDSS with large $d_{\rm BPT}$ measurements but low D_n4000. The lack of low-$d_{\rm BPT}$ objects at high D_n4000 suggests that the quiescent galaxies lack even the low level star formation seen in the quasi-quiescent galaxies. Upper panel: the number of BPT-quiescent galaxies as a function of D_n4000 in isolated (orange) and non-isolated (blue) environments. The presence of BPT-Q satellite galaxies in the same mass range indicates that we are not missing a hidden population of BPT-Q isolated galaxies.

lower along the AGN mixing sequence relative to their quiescent galaxy counterparts.

For comparison, the gray contours in Figure 6 show the full sample of low-mass isolated galaxies, with $d_{\rm BPT}$ values calculated from the SDSS emission line fluxes. The majority of galaxies have $D_n4000 < 1.5$ and scatter about $d_{\rm BPT} = 0$. This is in direct contrast to quiescent and quasi-quiescent galaxies, where we see a clear relation between $d_{\rm BPT}$ and D_n4000.

Though we attempted to randomly select galaxies from the SF population, all seven galaxies lie above $d_{\rm BPT} = 0$ even within the 3″ fiber, an unfortunate byproduct of a small sample size.

Two galaxies have SDSS-derived D_n4000 values indicative of star formation, but significantly elevated $d_{\rm BPT}$ (white squares in Figure 6). Both galaxies have SDSS emission line ratios that place them in the LINER region of the BPT diagram. However, the galaxies lie well outside the range of typical BPT-LINER values. Given these unphysical values, we plan follow-up spectroscopic observations of these galaxies before further classifying.

Thus far, we have relied on the [N II] BPT diagram to disentangle emission from star formation versus non-H II-region sources. The most commonly invoked explanation for non-SF-driven emission is an actively accreting black hole, but this is not the only possible source for the observed line ratios. The AGN region of the BPT diagram is known to host two distinct populations: Seyfert AGNs and low-ionization emission regions (commonly referred to as LINERs when found in the nuclear regions of galaxies). The two populations cannot be distinguished in the composite or near-composite regions of the BPT diagram, though Seyfert galaxies tend to have lower [N II]/Hα and higher [O III]/Hβ than LINERs.

Shocked gas from outflows can produce AGN-like line ratios, but it is unclear if such low-mass galaxies are capable of producing sufficiently energetic episodes of star formation (Dashyan et al. 2018). Studies of ionization sources on the BPT diagram (e.g., Yan & Blanton 2012; Belfiore et al. 2017) have found that heating from pAGB stars can mimic a low-accretion-rate black hole and produce LINER-like emission. However, the majority of our AGN candidates have central emission line ratios that are strongly characteristic of Seyfert AGN, rather than LINERs. Moreover, in the majority of cases, the Hα emission does not directly trace the stellar continuum, suggesting that an old stellar population is not the origin of the ionizing radiation.

5. Are We Missing Isolated Quiescent Galaxies?

$d_{\rm BPT}$ is a useful metric for parameterizing AGN strength in galaxies. However, truly quiescent galaxies (without any line emission) cannot be placed on the BPT diagram and lack $d_{\rm BPT}$ values. To confirm that we are not missing a population of fully quiescent isolated galaxies, we build a comparison sample of low-mass non-isolated galaxies from the NSA catalog. We define non-isolated galaxies as those with $D_{\rm host} =$ 0.4–1.0 Mpc. We add a lower bound to $D_{\rm host}$ to remove any actively merging or cluster galaxies and set the upper bound to ensure an equal number of non-isolated and isolated galaxies.

For both samples, we identify the sub-population of galaxies that are BPT-quiescent and have quiescent stellar populations. We consider galaxies to be BPT-quiescent if their SDSS spectra show well-detected Hα absorption lines (S/N (Hα) > 2). Based on the SDSS fiber measurements, we identify 97 non-isolated galaxies that are fully quiescent and only 3 isolated galaxies (this includes NSA 18953, whose absorption-dominated status is confirmed with our SDSS spectra). The large discrepancy between the two populations, despite the fact that they are drawn from equally sized parent samples in the same mass range confirms that SDSS would have identified any missing truly quiescent population of low-mass isolated galaxies. We show the SDSS-defined truly quiescent population for both isolated and satellite galaxies in the upper panel of Figure 6.

6. Discussion

We find evidence for AGN-like line ratios in the majority of isolated, low-mass, quiescent galaxies observed in this study. We suggest several explanations for quenching in this regime in order to motivate further studies of host galaxy and AGN properties which could distinguish between the possible scenarios.

The internal feedback processes needed to remove or heat gas in isolated quiescent galaxies could be unrelated to AGN. In this scenario, we would expect the AGN fraction in SF isolated galaxies to be similar to the quenched population, or perhaps higher due to more available gas. Trump et al. (2015) showed that dilution due star formation will significantly bias against finding AGNs via BPT line ratios in lower mass SF galaxies. In this scenario, we predict the true AGN fraction (determined via higher spatial resolution spectroscopy or multiwavelength studies) in isolated SF galaxies is similar to that of the quenched galaxies. If this is not the case, we must

provide a different explanation for why the majority of quiescent galaxies are observed to have AGN-like line ratios.

Alternatively, AGN feedback could be the underlying quenching mechanism for the low-mass quiescent galaxies in isolation. In this scenario, AGN either drive the permanent depletion of the internal gas reservoir or cause burst-like periods of quiescence driven by particularly energetic episodes of AGN activity. In the case of permanent quiescence, a slow quenching timescale or additional mechanisms disrupting the gas reservoir prior to quenching would be required to explain the low number of quiescent galaxies relative to the known population of SF galaxies hosting AGN. Star formation histories could distinguish between a slow and permanent quenching process versus a shorter-timescale bursty quenching cycle.

7. Summary

In this work, we investigate the connection between AGN-like line ratios and quiescence in low-mass, isolated galaxies. We have acquired high-resolution, spatially resolved spectroscopy for 27 isolated low-mass galaxies, and measured key optical emission lines as a function of radius. We are able to place 25 of 27 galaxies on the BPT diagram in a spatially resolved manner. Within the central $1''$ of each galaxy, we measure the galaxy's distance from the SF sequence in BPT-space ($d_{\rm BPT}$). We use this parameter as a measure of AGN activity within a galaxy. Our results are summarized as follows:

1. We qualitatively distinguish a variety of trends in the radial BPT diagram for galaxies in our sample. We find a significant number of quiescent galaxies have extended emission, which forms distinct tracks in BPT-space, moving from the SF or composite regions at $R \sim R_{\rm eff}$ to the AGN region in the galaxy center (Figure 3, as well as Appendix Figures 7–9).
2. We identify central non-SF ionizing radiation in 16 of 20 quiescent and quasi-quiescent galaxies (Figure 5).
3. We find that almost all isolated quiescent galaxies host AGNs, in contrast to denser environments, where we find significant numbers of quiescent galaxies without AGN-like line ratios.

While we cannot confirm that AGNs are actively quenching the galaxies in our sample, the ubiquity of AGN-like line ratios in low-mass quiescent galaxies adds to the growing body of evidence that AGNs play a crucial role in self-quenching galaxies at all mass scales. Careful follow-up with both radio and X-ray facilities will be crucial for confirming the presence of AGNs within these systems.

Additionally, constraining the ages of the quiescent and quasi-quiescent galaxies in our sample will help build up a coherent picture of the quenching process at play. In this work, we have used the 4000 Å break to trace the mean light-weighted age of stellar populations in galaxies. D_n4000 is an effective method for identifying recent ($\sim$1–3 Gyr) bursts of star formation, but becomes insensitive to older stellar ages (e.g., 7 versus 13 Gyr), particularly at low metallicities (Kauffmann et al. 2003b).

The measurement of spatially resolved star formation histories for our sample of low-mass isolated galaxies will provide significant insight into the quenching process at work. Future work will explore the spatially resolved SF histories as well as the kinematics of both the gas and stars as derived from our ESI observations in order to constrain the nature of AGN feedback within low-mass, isolated galaxies.

We thank the anonymous referee for their insightful feedback which has strengthened the paper. C.M.D. thanks Jenny Greene, Vivienne Baldassare, and Michael Tremmel for their helpful comments on this work. M.G. acknowledges support from the National Science Foundation under AST grant No. 1517422 and the Howard Hughes Medical Institute (HHMI) Professors Program. A.W. is supported by a Caltech-Carnegie Fellowship, in part through the Moore Center for Theoretical Cosmology and Physics at Caltech, and by NASA, through ATP grant 80NSSC18K1097 and *HST* GO-14734 and AR-15057 from STScI. K.E.B. acknowledges support from an NSF graduate research fellowship.

Appendix A
Spatially Resolved BPT Diagrams

We present the spatially resolved BPT diagrams for the remaining 21 galaxies in the sample. Figure 7 shows the galaxies classified as having quiescent stellar populations in SDSS; Figure 8 shows the quasi-quiescent galaxies; and Figure 9 shows the star forming galaxies. In each panel, the spectrum extracted from the central 1" is circled in blue, and all points are color-coded with distance from the galaxy center.

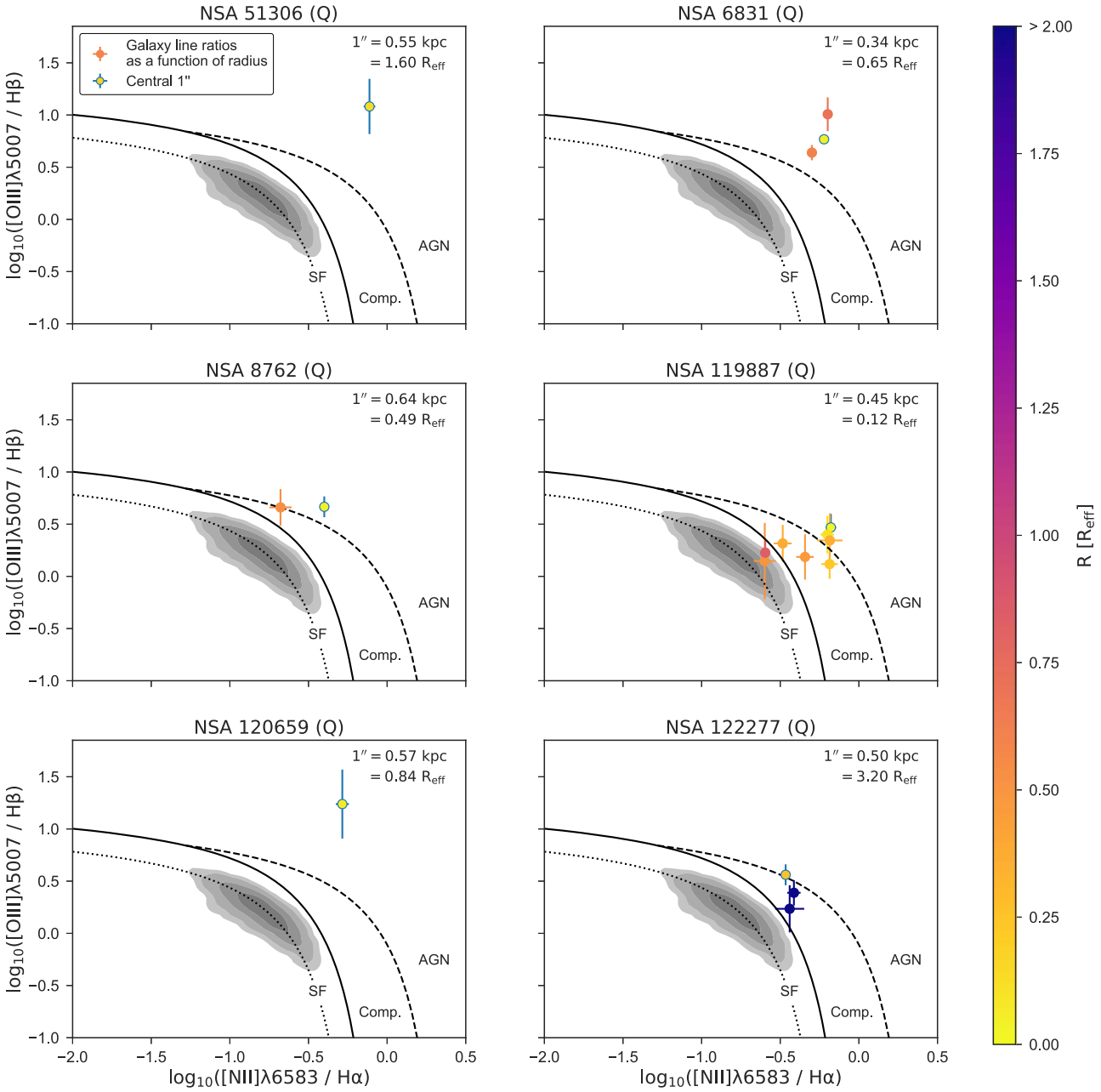

Figure 7. BPT diagrams for quiescent galaxies in our sample. Each panel shows the locus of low-mass isolated galaxies with well-measured BPT emission lines (Hα and Hβ S/N $>$ 3) from the NASA/Sloan Atlas (NSA; gray contours) as well as the demarcation lines between sources of ionizing radiation as given in Kewley et al. (2013), where the dotted line traces the median [H II] abundance sequence, the solid line is the empirical delineation between star formation and AGN (Kauffmann et al. 2003a), and the dashed line is the maximum-starburst line (Kewley et al. 2001). We show BPT measurements derived from the ESI spectra as circles, color-coded by distance from the galaxy center.

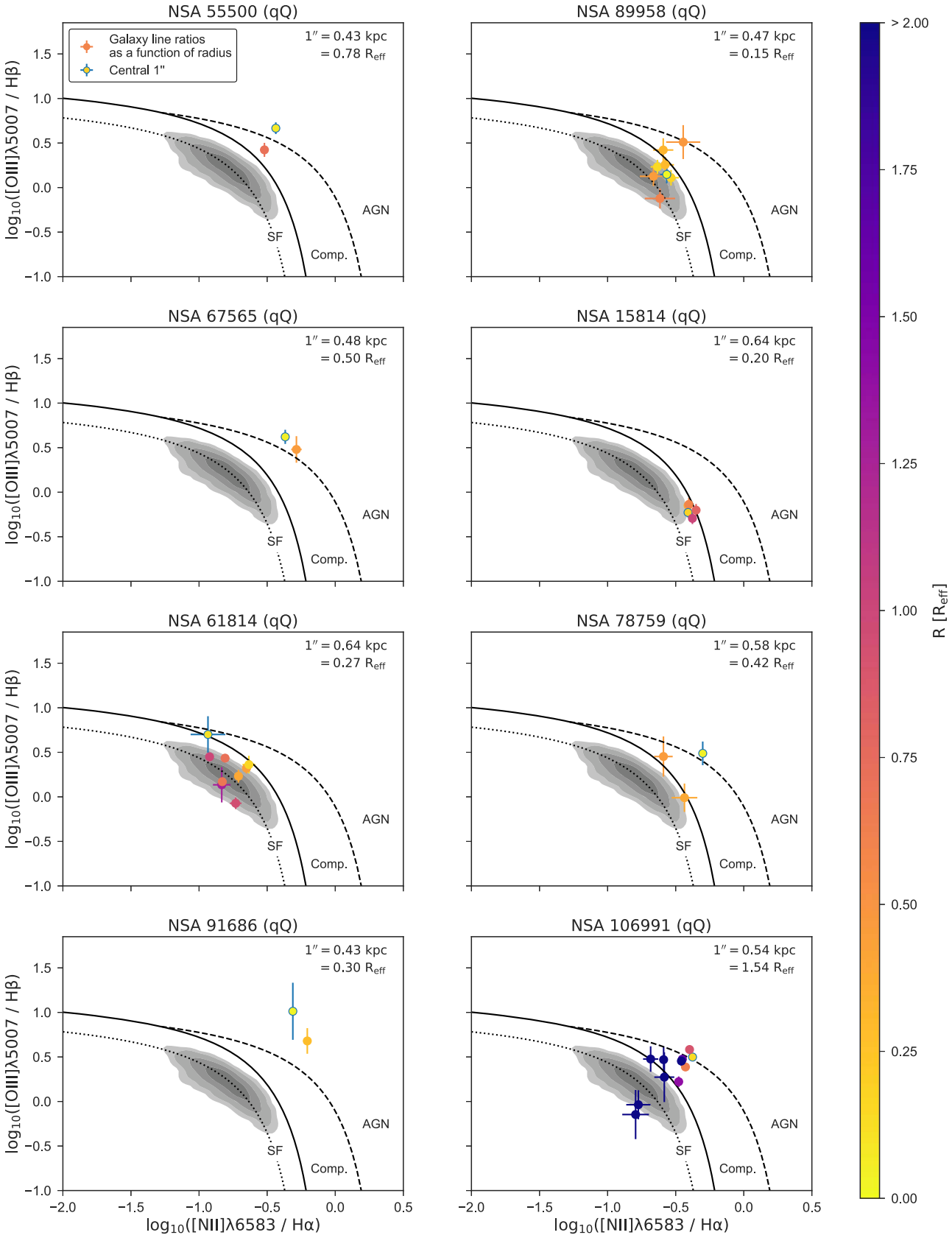

Figure 8. Same as Figure 7, for quasi-quiescent galaxies.

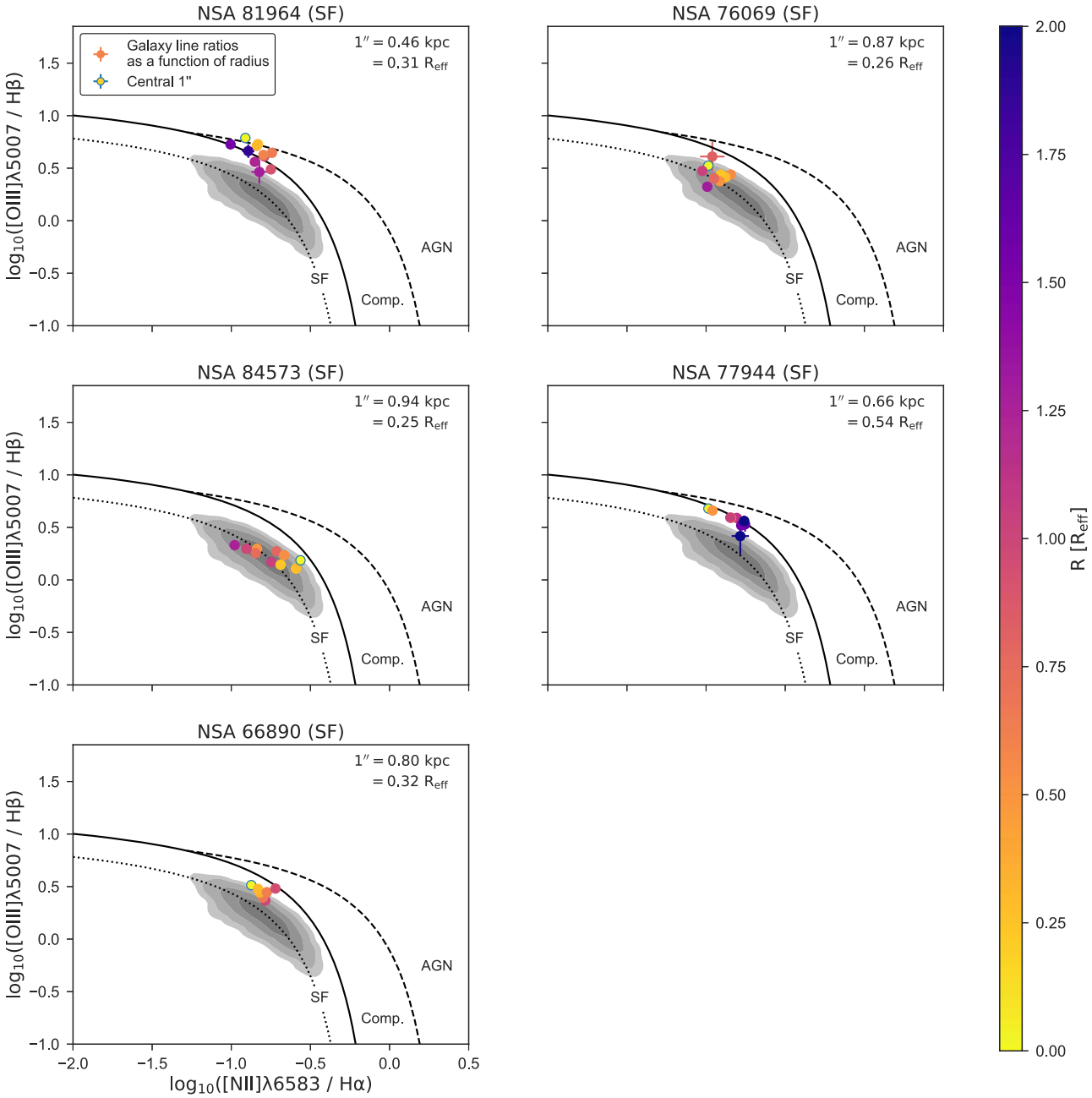

Figure 9. Same as Figure 7, for SF galaxies.

ORCID iDs

Claire Mackay Dickey https://orcid.org/0000-0002-1081-3991
Marla Geha https://orcid.org/0000-0002-7007-9725
Andrew Wetzel https://orcid.org/0000-0003-0603-8942
Kareem El-Badry https://orcid.org/0000-0002-6871-1752

References

Agostino, C. J., & Salim, S. 2019, ApJ, 876, 12
Aihara, H., Allende Prieto, C., An, D., et al. 2011, ApJS, 193, 29
Baldassare, V. F., Geha, M., & Greene, J. 2018, ApJ, 868, 152
Baldassare, V. F., Reines, A. E., Gallo, E., et al. 2016, ApJ, 829, 57
Baldassare, V. F., Reines, A. E., Gallo, E., & Greene, J. E. 2015, ApJL, 809, L14
Baldwin, J. A., Phillips, M. M., & Terlevich, R. 1981, PASP, 93, 5
Balogh, M. L., Morris, S. L., Yee, H. K. C., Carlberg, R. G., & Ellingson, E. 1999, ApJ, 527, 54
Barth, A. J., Greene, J. E., & Ho, L. C. 2008, AJ, 136, 1179
Barth, A. J., Ho, L. C., Rutledge, R. E., & Sargent, W. L. W. 2004, ApJ, 607, 90
Belfiore, F., Maiolino, R., Tremonti, C., et al. 2017, MNRAS, 469, 151
Blanton, M. R., Kazin, E., Muna, D., Weaver, B. A., & Price-Whelan, A. 2011, AJ, 142, 31
Blanton, M. R., & Roweis, S. 2007, AJ, 133, 734
Bower, R. G., Benson, A. J., Malbon, R., et al. 2006, MNRAS, 370, 645
Bower, R. G., Schaye, J., Frenk, C. S., et al. 2017, MNRAS, 465, 32
Bradford, J. D., Geha, M. C., Greene, J. E., Reines, A. E., & Dickey, C. M. 2018, ApJ, 861, 50
Byler, N., Dalcanton, J. J., Conroy, C., & Johnson, B. D. 2017, ApJ, 840, 44
Cann, J. M., Satyapal, S., Abel, N. P., et al. 2019, ApJL, 870, L2
Cappellari, M. 2017, MNRAS, 466, 798
Chabrier, G. 2003, PASP, 115, 763
Choi, E., Ostriker, J. P., Naab, T., Oser, L., & Moster, B. P. 2015, MNRAS, 449, 4105

Conroy, C., & Gunn, J. E. 2010, ApJ, 712, 833
Conroy, C., Gunn, J. E., & White, M. 2009, ApJ, 699, 486
Croton, D. J., Springel, V., White, S. D. M., et al. 2006, MNRAS, 365, 11
Dashyan, G., Silk, J., Mamon, G. A., Dubois, Y., & Hartwig, T. 2018, MNRAS, 473, 5698
Dekel, A., & Silk, J. 1986, ApJ, 303, 39
El-Badry, K., Wetzel, A., Geha, M., et al. 2016, ApJ, 820, 131
Filippenko, A. V., & Ho, L. C. 2003, ApJL, 588, L13
Gabor, J. M., Davé, R., Oppenheimer, B. D., & Finlator, K. 2011, MNRAS, 417, 2676
Geha, M., Blanton, M. R., Yan, R., & Tinker, J. L. 2012, ApJ, 757, 85
Genel, S., Vogelsberger, M., Springel, V., et al. 2014, MNRAS, 445, 175
Graus, A. S., Bullock, J. S., Fitts, A., et al. 2019, arXiv:1901.05487
Greene, J. E., & Ho, L. C. 2007, ApJ, 670, 92
Groves, B. A., Heckman, T. M., & Kauffmann, G. 2006, MNRAS, 371, 1559
Kauffmann, G., Heckman, T. M., Tremonti, C., et al. 2003a, MNRAS, 346, 1055
Kauffmann, G., Heckman, T. M., White, S. D. M., et al. 2003b, MNRAS, 341, 33
Kewley, L. J., Dopita, M. A., Sutherland, R. S., Heisler, C. A., & Trevena, J. 2001, ApJ, 556, 121
Kewley, L. J., Groves, B., Kauffmann, G., & Heckman, T. 2006, MNRAS, 372, 961
Kewley, L. J., Maier, C., Yabe, K., et al. 2013, ApJL, 774, L10
Kormendy, J., & Kennicutt, R. C. J. 2004, ARA&A, 42, 603
Kroupa, P. 2001, MNRAS, 322, 231
Martín-Navarro, I., & Mezcua, M. 2018, ApJL, 855, L20
Papovich, C., Kawinwanichakij, L., Quadri, R. F., et al. 2018, ApJ, 854, 30
Pasquali, A., Gallazzi, A., Fontanot, F., et al. 2010, MNRAS, 407, 937
Peng, Y.-j., Lilly, S. J., Kovač, K., et al. 2010, ApJ, 721, 193
Penny, S. J., Masters, K. L., Smethurst, R., et al. 2018, MNRAS, 476, 979
Prochaska, J. X., Gawiser, E., Wolfe, A. M., Cooke, J., & Gelino, D. 2003, ApJS, 147, 227
Reines, A. E., Greene, J. E., & Geha, M. 2013, ApJ, 775, 116
Sartori, L. F., Schawinski, K., Treister, E., et al. 2015, MNRAS, 454, 3722
Satyapal, S., Vega, D., Heckman, T., O'Halloran, B., & Dudik, R. 2007, ApJL, 663, L9
Schaye, J., Crain, R. A., Bower, R. G., et al. 2015, MNRAS, 446, 521
Sheinis, A. I., Bolte, M., Epps, H. W., et al. 2002, PASP, 114, 851
Smith, R. J., Lucey, J. R., Price, J., Hudson, M. J., & Phillipps, S. 2012, MNRAS, 419, 3167
Somerville, R. S., & Davé, R. 2015, ARA&A, 53, 51
Somerville, R. S., Hopkins, P. F., Cox, T. J., Robertson, B. E., & Hernquist, L. 2008, MNRAS, 391, 481
Su, K.-Y., Hopkins, P. F., Hayward, C. C., et al. 2019, MNRAS, 487, 4393
Trump, J. R., Sun, M., Zeimann, G. R., et al. 2015, ApJ, 811, 26
van de Weygaert, R., & Platen, E. 2011, IJMPS, 1, 41
van Dokkum, P. G. 2001, PASP, 113, 1420
Veilleux, S., & Osterbrock, D. E. 1987, ApJS, 63, 295
Wetzel, A. R., Tinker, J. L., Conroy, C., & van den Bosch, F. C. 2013, MNRAS, 432, 336
White, S. D. M., & Frenk, C. S. 1991, ApJ, 379, 52
White, S. D. M., & Rees, M. J. 1978, MNRAS, 183, 341
Yan, R. 2011, AJ, 142, 153
Yan, R. 2018, MNRAS, 481, 476
Yan, R., & Blanton, M. R. 2012, ApJ, 747, 61